Cellular pattern dynamics on a concave interface in three-dimensional alloy solidification

C. Weiss, N. Bergeon, N. Mangelinck-Noël, and B. Billia
Aix Marseille Université and CNRS, UMR 6242, IM2NP, Campus Scientifique de Saint-Jérôme, Case 142, 13397 Marseille Cedex 20, France

(Received 2 June 2008; revised manuscript received 22 September 2008; published 22 January 2009)

Three-dimensional interface patterns are common in condensed matter, whose dynamical behavior is still deserving clarification. The dynamics of cellular patterns formed at the concave solid-liquid interface during directional solidification in a cylinder of a transparent alloy is studied by means of bright-field live imaging. For each pulling velocity, *in situ* observation shows that the asymptotic cellular pattern, which establishes with time, is characterized by the continuous birth of a large number of cells at a circular source of morphological instability on the periphery, the sustained collective gliding of the whole cellular array down the interface slope, and the elimination of coarse cells at the central sink. This very peculiar dynamics is the specific signature of the cell advection imposed by interface curvature for the concave situation in three-dimensional solidification. It follows from the comparison between experimental cell gliding and pure slope advection that an additional mechanism of pattern advection is active. It is attributed to fluid flow interaction, estimated on the basis of the Forth and Wheeler traveling wave equations.

DOI: 10.1103/PhysRevE.79.011605 PACS number(s): 81.10.Fq, 05.65.+b, 81.30.Fb

I. INTRODUCTION

The topic of pattern formation is of paramount importance in many fields of sciences, and the process of pattern selection is quite complex since it occurs in a highly nonlinear growth regime [1]. During directional solidification of alloys, the interface between the solid and the melt exhibits complex patterns that are analogous to patterns that form in other fields such as combustion, fluid dynamics, geology, and biology. Three-dimensional patterns are often either not stable or difficult to study experimentally in a quantitative manner. In contrast, solidification patterns in three dimensions can be accurately studied through directional solidification experiments, and the understanding of solidification patterns will provide a general theoretical framework for a broader problem of pattern formation in nature.

Moreover, it is long recognized that materials properties are largely controlled by the microstructure formed in the solid during processing, so that the precise mastering of its development during solidification is essential to reproducibly tailor products of specified quality. It is therefore necessary to unceasingly deepen the quantitative understanding of the basic physical principles that, from the microscopic to the macroscopic scales, govern microstructure formation.

Directional solidification (Bridgman type) is one of the key techniques for the precise study of the fundamental aspects of solidification since the control of the experimental parameters is accurate and can be done independently. For an alloy of a given solute concentration C_0, an experiment is controlled by the thermal gradient G and the pulling velocity V_P. If the gradient G is furthermore fixed, the planar solid-liquid interface undergoes morphological instability as the applied velocity is increased beyond a critical value which leads to the development of cellular, and then dendritic, microstructures. In practice, in experiments the planar solid-liquid interface bifurcates into cellular structure during the initial solidification transient when the instantaneous control parameter, proportional to V_iC_i/G with V_i and C_i the instantaneous interface velocity and liquid concentration at the interface, respectively, exceeds the onset value for morphological instability [2]. The dynamics of formation of solidification patterns is commonly studied using transparent organic systems that solidify like metals, so that *in situ* observation of growth is possible in real time. On such systems, directional solidification studies are usually conducted in a configuration where the sample is constrained between two narrowly spaced plates, thus corresponding to a quasi-two-dimensional (2D) configuration.

A recent study on such samples has pointed out a phenomenon of cell advection when a controlled macroscopic curvature, convex in that case, was purposely imposed to the interface [3]. Cell stretching was evidenced while the cells were drifting along the interface, which induced nucleation of new cells by repetitive tip splitting. The self-organization into a time-dependent but regular cellular pattern was thoroughly analyzed by Pocheau and Bottin-Rousseau [4], who elaborated a phase-dynamics model and showed the existence of a periodic attractor. This study has demonstrated the possibility of imposing regularity in pattern organization at array length scale (cell size) by acting at much larger length scale (macroscopic interface). Practically, in usual experimental conditions [three-dimensional (3D) configurations], solidification fronts are most generally curved, which stresses the importance of unveiling the effects driven by interface curvature in the dynamical formation, selection, and organization of the solid-liquid interface microstructure. We here report striking results obtained on transparent samples, in a 3D configuration where the solid-liquid interface is naturally concave. In that case, it appears that cellular array dynamics is drastically modified by curvature, but it is also affected by interactive coupling with fluid flow in the adjacent melt. In particular, a lateral drift of the cellular array is evidenced. The evolution of cells from their birth until their elimination during their gliding towards the interface center is characterized from *in situ* and real-time optical observation. Cell size variation is also analyzed, and the influ-

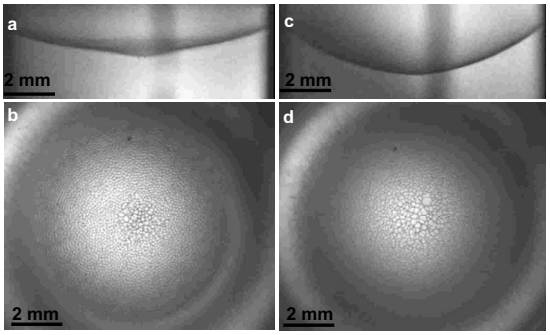

FIG. 1. (a) Side view and (b) top view of the interface for $V_P = 10\ \mu$m/s. (c) Side view and (d) top view of the interface for $V_P = 20\ \mu$m/s. SCN 0.3 wt. % water; $G = 30$ K/cm.

ence of other phenomena, such as array dynamics, is discussed.

II. EXPERIMENTAL PROCEDURE

For the present study, we used the directional solidification insert (DSI) dedicated to the *in situ* and real time characterization of the solid-liquid interface on bulk samples of transparent materials, developed by the French Space Agency (CNES) for the DECLIC facility. A succinonitrile (SCN) 0.3 wt. % water alloy is contained in a cylindrical glass tube with an inner diameter of 10 millimeters and a length that enables about 10 centimeters of solidification. Before filling the crucible, the SCN is first distillated at least twice, and the alloy is then prepared by adding the solute. The crucible is equipped with a flat glass window at the bottom and a lens immersed in the melt at the top so that the observation of the interface can be performed from the top. Additionally, the interface can also be observed from the side. A thermal gradient of 10–30 K cm^{-1} is imposed by regulated hot and cold zones, respectively, located above and below the adiabatic area where the interface is positioned. Upward solidification is achieved by pulling the crucible down into the cold zone of the furnace at a rate ranging from 0.1 to 20 μm/s. A more detailed description of this device can be found in Refs. [5,6].

At rest ($V_P = 0$), the macroscopic interface shape is imposed by the shape of the isotherms in the adiabatic area and is almost flat (the height variation between the center and the border of the interface is below 0.3 mm, which is negligible compared to the curvatures that we will discuss later). When solidification begins, this shape is progressively changing during the initial transient due to latent heat generation. In metallic systems, a natural convex interface is generally obtained while pulling due to the significantly higher heat conductivity of solid phase compared to liquid; in the case of succinonitrile based alloys, the situation is quite different as the thermal conductivities of the two phases are almost identical but significantly lower than that of the glass crucible. The evacuation of the latent heat is thus more efficient on the periphery, through the crucible, leading to the formation of a negative radial temperature gradient and a macroscopic concave interface [Figs. 1(a) and 1(c)]. The amplitude of the curvature is directly related to the pulling rate that controls the rate of latent heat generation. Moreover, the radial thermal gradient is driving fluid flow, ascending in the center of the crucible and descending near the wall. Consequently, the solute boundary layer adjacent to the solid-liquid interface in alloy solidification is swept by fluid flow so that the solute concentration is greater in the center, inducing concomitant local recoil of the interface position due to the local decrease of the equilibrium interface temperature. It follows that the normal gradient of concentration, which depends on the local solute concentration and normal growth velocity, varies along the curved interface so that the local value of the cellular threshold, which is also a function of the normal temperature gradient, varies as well. The ultimate result is the noticeable radial gradient of interface microstructure from the border to the center of the crucible. In particular, localization of the cellular microstructure, typical of a convection mode driven by the radial temperature gradient [7], is clearly observed in Figs. 1(b) and 1(d) where a disk of cells is surrounded by a smooth ring. It should be noticed that the cells are actually very shallow; they can hardly be distinguished in transverse view near the center in Figs. 1(a) and 1(c). Besides, solute accumulation in the stagnation region below ascending fluid flow may result in an interface pit [Fig. 1(a)]; such shape-distortion phenomena directly resulting from convection structure have been pointed out in both experiments and numerical simulation [7–9].

In the figure captions, for solute concentration we merely refer to the nominal concentration of the alloy set in filling the cartridge and the values of the thermal gradients correspond to those measured in a test sample of pure SCN solidified in a crucible equipped with thermocouples, with the same temperatures applied to the furnace zones. Yet, the significant nonuniformity of the solid-liquid interface microstructure suggests that the impossibility of local measurement of temperature, solute concentration, and flow velocity may strongly limit, if not preclude, the quantitative analysis of results. To circumvent this difficulty we rely on numerical simulation of both thermal field and fluid flow performed using the CrysVUn® software that is designed for the global modeling of solidification processes [10,11]. These calculations are based on a method of finite volumes on unstructured grids that enables us to tackle the entire growth setup on the basis of a geometrical model of the furnace, crucible, and sample and assignment of the relevant physical properties to all materials involved in this setup. The temperatures applied to the different elements of the furnace, pulling rates and sample composition are entered as input parameters for the numerical simulations. Examples of results will be given in Fig. 5.

III. INTERFACE CURVATURE AND PATTERN ADVECTION

A. Experimental results

The dynamics of the cellular patterns in Fig. 1 are now analyzed. *In situ* and real-time observation shows that, for all pulling velocities, the cellular patterns that develop during the transient stages reach asymptotic states characterized by

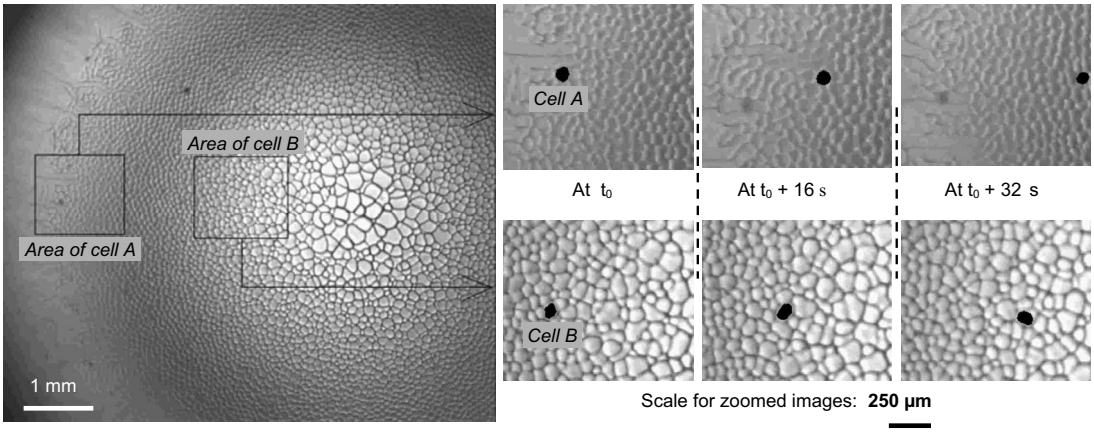

FIG. 2. Motion of two cells located in different areas of the interface. SCN 0.3 wt. % water, V_P=20 μm/s, G=30 K/cm.

permanent and regular dynamics: A number of cells continuously form at the circular boundary between unstable area and smooth interface; they glide collectively down the interface slope, and many of them get eliminated while moving, especially around the center of the interface where the coarsening process is active; the surviving coarse cells finally disappear in a central sink. A representative example of this phenomenon is given in a video [12]. This very specific dynamics is the signature of advection imposed by interface curvature on the usual microstructure dynamics. It is here observed for the concave situation, in three-dimensional solidification and in interaction with fluid flow. This happens because (i) the normal to the solid-liquid interface is at an angle with the vertical pulling direction, (ii) crystalline anisotropy is weak in succinonitrile-based alloys so that the cell growth direction is not yet constrained to approach a ⟨100⟩ direction as it is commonly observed for dendrites growing at velocities well above the onset of morphological instability, and (iii) the cells (tips and shallow grooves) grow in the direction of the thermal gradient which is identified to the normal to the interface (this assumption leads us to consider that the interface follows an isotherm, so that concentration variations that effect equilibrium temperature are neglected) [4]. Cell advection is illustrated in Fig. 2 where two different cells are followed along their motion. The variation of the radial gliding rate of cells along their motion $V_{rA}(r)$, deduced from videos, is reported in Fig. 3 for V_P=10 and 20 μm/s. The radial gliding velocity of individual cells is deduced from their displacement in a short time interval (see, e.g., Fig. 2) and each experimental data point in Fig. 3 corresponds to an average of local drift measurements on several cells starting from the same radial position all around the interface. The dispersion of the data points gives an estimate of measurement accuracy. On the whole, the variation of V_{rA} from the circular cell source on the periphery exhibits a smooth decrease terminated by a sharp drop in the central sink. The physical mechanisms responsible for this evolution are analyzed and discussed in the following.

B. Analysis of the advection by the interface slope

Let us first calculate in cylindrical coordinates $(\vec{u}_r, \vec{u}_\theta, \vec{u}_z)$ the gliding of the cells due to the interface slope, as seen in view from the top. Figure 4(a) gives a schematic representation of the concave solid-liquid interface and a specific cell at two successive times t and $t+dt$.

The vertical interface velocity and cell growth velocity along the normal are, respectively, denoted $\mathbf{V_P}$ and $\mathbf{V_n}$. In the absence of any other driving force, top observation of the interface should show slope-induced cell gliding towards the center with a velocity $\mathbf{V_{rA,s}}$ that can simply be expressed as

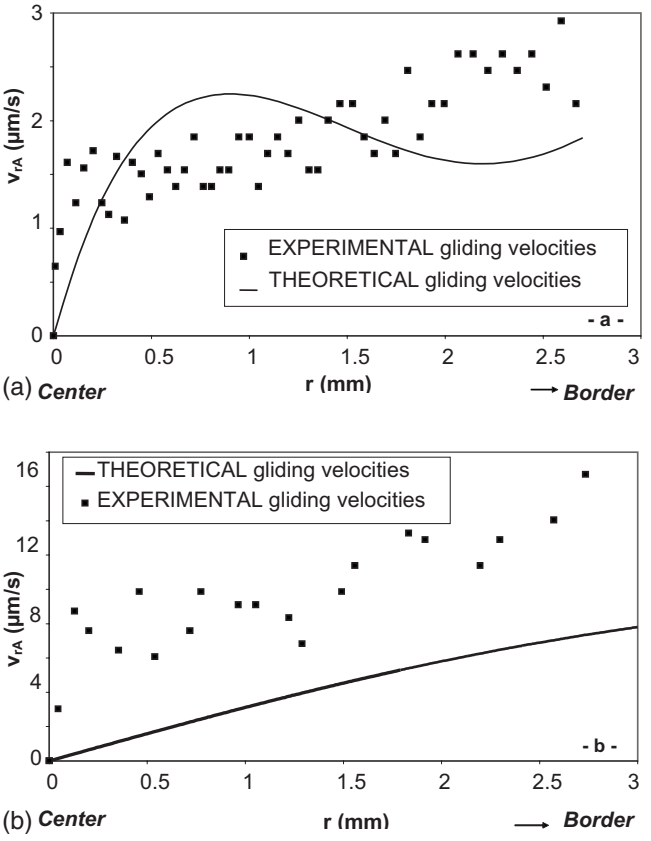

FIG. 3. Radial gliding velocities V_{rA} along the interface for (a) V_P=10 μm/s and (b) V_P=20 μm/s. In both cases, theoretical calculations of $V_{rA,s}$ based on slope advection are superposed to experimental measurements of V_{rA}, thus pointing out the existence of an additional contribution responsible for the discrepancy.

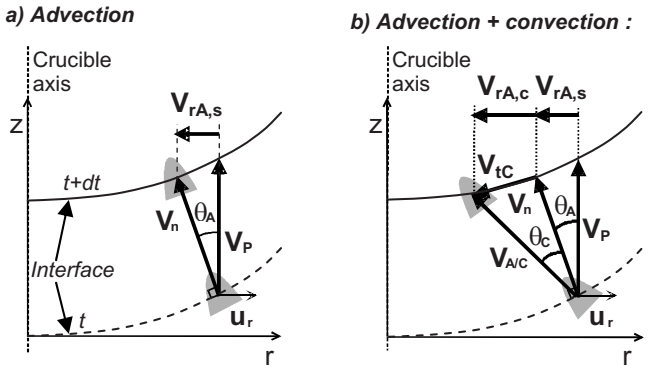

FIG. 4. Cell growth on a concave solid-liquid interface (dt =unit time) showing the various velocity contributions to cell advection: (a) Advection by the interface slope, (b) advection enhancement by fluid flow.

a function of $\mathbf{V_P}$ and the angle θ_A between the growth direction and the interface normal,

$$\overrightarrow{V_{rA,s}} = -V_P \cos\theta_A \sin\theta_A \vec{u}_r. \tag{1}$$

As the solid-liquid interface is to a good approximation axisymmetric in experiments, its shape can be described by a function $z_i=f(r)$ so that

$$\overrightarrow{V_{rA,s}} = -V_P \frac{dz_i/dr}{1+(dz_i/dr)^2}\vec{u}_r. \tag{2}$$

It follows from Eq. (2) that $\mathbf{V_{rA,s}}$ is a function of r as the local interface slope, dz_i/dr, varies all along the interface. In practice, Eq. (2) is used to determine the theoretical cell gliding velocity $V_{rA,s}(r)$ on the basis of the experimental interface shapes of Figs. 1(a)–1(c), at pulling rates 10 and 20 μm/s, respectively. The values obtained for $V_{rA,s}(r)$ are then compared to the experimental measurements of $V_{rA}(r)$.

The macroscopic interface shape at $V_P=20$ μm/s (Fig. 1) can be correctly fitted by a parabola and the theoretical variation predicted by Eq. (2) shows a monotonous decrease of the advection velocity $V_{rA,s}$—due to the decrease of interface slope—when approaching the center of the crucible [Fig. 3(b)]. A large, and about constant, misfit between $V_{rA,s}$ and V_{rA} is noticeable that brings out that cell gliding in experiments cannot be entirely ascribed to cell advection driven by the interface slope. The interface at $V_P=10$ μm/s, which deviates from a simple parabola due to the central pit caused by solute accumulation, was fitted by a fifth-order polynomial to correctly reproduce its somewhat complex shape. It follows that the evolution of $V_{rA,s}$ is not monotonous [Fig. 3(a)]. On the one hand, the increase of $V_{rA,s}$ from $r=2$ to 0.9 mm is not reflected in the experimental data points, so that the fair quantitative agreement must be considered with care, all the more as this corresponds to the pit region where the validity of the assumption that the direction of the thermal gradient is identical to the normal to the interface is the more questionable. On the other hand, in the beginning of the drift of the cell array ($r>2$ mm), a misfit similar to that at V_P =20 μm/s is observed. The origin of this misfit will be first sought for in the light of available experimental results [13] and theoretical predictions [14–17], which both suggest to attribute the initial discrepancy between $V_{rA,s}$ and V_{rA} to the interaction with convection.

C. Influence of convection

On the experimental side, it is long known that fluid flow parallel to a growing dendritic interface strongly alters the dendrite shape, generating a tilting of growth direction upstream [18]. In their systematic study under imposed controlled flow, Huang *et al.* [13] report a similar tilting for a cellular interface but in the direction opposite to that in dendritic growth, i.e., downstream inclination. In both cases, convection effect is to sweep the solute boundary layer along the interface with the main difference that fluid flow is penetrating the porous mushy zone, where the dendrites are individually acting as obstacles. It results that, in case of a dendritic array, the isoconcentration lines are packed on the upstream side of dendrite stalks, leading to preferential growth and concomitant enhancement of sidebranching there [19]. As the porosity of the cellular array is low, and thus flow penetration into the mush to first-order negligible, solute is essentially swept downstream. Under diffusion transport, the solute field adjacent to the interface is modulated according to the distribution of the cell tips and grooves, which, respectively, impose minima and maxima in the solute concentration at the interface. The presence of fluid flow makes this modulated solute field drifting downstream as a traveling wave that carries on the cellular interface with it [14] and sets the cell growth direction beyond that imposed by the local temperature gradient [Fig. 4(b)]. In practice, this glide V_{tC} of the tip position tangential to the interface induces a supplementary advection $V_{rA,c}$ in interface top view [Fig. 4(b)]. The geometric analysis leads to the following expression for $V_{rA,c}$ as a function of either V_{tC} or the angle θ_C between the cell growth velocity $V_{A/C}$, which includes both slope and fluid-flow advections, and the normal growth velocity V_n:

$$\overrightarrow{V_{rA,c}} = V_{tC}\cos\theta_A\vec{u}_r = -V_P\cos^2\theta_A\tan\theta_C\vec{u}_r. \tag{3}$$

Then, the total glide $\mathbf{V_r}$ is the sum of the slope advection and convection advection contributions,

$$\vec{V}_r = \left(-\frac{V_P\dfrac{dz_i}{dr}}{1+\left(\dfrac{dz_i}{dr}\right)^2} + \frac{V_{tC}}{\sqrt{1+\left(\dfrac{dz_i}{dr}\right)^2}}\right)\vec{u}_r$$

$$= -\frac{V_P\dfrac{dz_i}{dr} + V_P\tan\theta_C}{1+\left(\dfrac{dz_i}{dr}\right)^2}\vec{u}_r. \tag{4}$$

Applying this analysis to the Huang *et al.* case in Fig. 6(b) [13], where $V_P=3.33$ μm/s, $\theta_C\approx 6°$ and $U_\infty=0.5$ mm/s, with $\theta_A=0$ so that Eq. (4) reduces to $V_r/V_P=\tan\theta_C$, it results that the supplementary glide $V_{rA,c}$ $(=V_{tC})$ was about 0.33 μm/s in the experiment, i.e., about 10% of the pulling rate.

On the theoretical side, the effects of forced flow on morphological instability were studied by analytical modeling and numerical simulation [14–17], showing that a flow parallel to the interface tends to stabilize perturbations (larger critical concentration than in the absence of flow) and may give rise to traveling waves. For example, Coriell *et al.* [16] carried out a linear stability analysis of the planar solid-liquid interface, including the calculation of the critical wavelength and wave speed, during the directional solidification of Pb-Sn alloys under a Couette flow. They report an increase of the wave speed with the flow rate calculated at the limit of diffusion boundary layer (length D/V_P with D the diffusion coefficient) (see Fig. 6 of [16]). Forth and Wheeler (FW) analysis [14] is the most relevant to the present experiments. In particular, these authors considered the influence of a boundary-layer flow parallel to the interface (asymptotic suction velocity profile) on morphological instability, and elaborated analytical solutions in the limit of large Schmidt number ($=\nu/D$ with ν the melt kinematic viscosity) and Reynolds number ($=U_\infty/V_P$ with U_∞ the fluid velocity far from the interface) of order one to evaluate the stabilizing or destabilizing effect of the flow, the direction (downstream or upstream) and the speed of the traveling wave at the onset of morphological instability. Consequently, we propose to describe our experimental situation in a way approaching the FW model, to estimate the additional cell advection velocity due to convection, and to compare it to the misfit between the theoretical and experimental gliding velocities (Fig. 3). We build our analysis on the analytical relationship Eq. (4.12) in Ref. [14], derived by FW to clarify the stabilizing or destabilizing effect of the flow on morphological instability, and calculate the direction (forward or backward) and the traveling wave speed at the onset of morphological instability. This relationship gives the wave speed of the disturbance that in our notations corresponds to the tangential velocity of the cell tips due to convection V_{tC}.

The FW model analyzes the onset of morphological instability so that we limit its use in the neighborhood of the cell source only, and not over the whole cellular interface as the level of morphological instability is continuously increasing while the cells are gliding from the source to the sink. For pulling rates of 10 and 20 μm/s, this region is, respectively, located about at $r=2.5$ mm and $r=3.5$ mm, and the corresponding cell size λ is, respectively, 73 μm and 71 μm.

In FW, the structure of the flow parallel to the interface is taken as an asymptotic suction profile that in our notations reads as

$$U_\parallel(d_n) = U_\infty[1 - \exp(-V_n d_n/\nu)] \tag{5}$$

with d_n the distance measured along the normal to the interface. In this expression, the length scale of the shear flow is ν/V_n, which is of the order of 0.1 m in the case of molten succinonitrile. Actually, in our experimental situation where the crucible radius R (=0.005 m) is much less than this length scale the variation of $U_\parallel$ with the distance d_n does not correspond to such a suction profile. Indeed, it follows from numerical simulations performed using the CrysVUn® software that the flow is obviously structured at the scale of the crucible confinement, as illustrated in Fig. 5(a) that shows a typical example of the actual structure of fluid flow along the curved interface for a pulling rate of 20 μm/s. However, in the vicinity of the solid-liquid interface, the flow can be approximated by a suctionlike profile by using the crucible radius R for the flow length scale and fitting the slope at the origin to the profiles $U_\parallel=f(d_n)$ extracted from CrysVUn® (taken at $r=2.5$ mm for $V_P=10$ μm/s and $r=3.5$ mm for $V_P=20$ μm/s [Fig. 5(c)]). Then, Eq. (5) becomes

$$U_\parallel(d_n) = U_\infty[1 - \exp(-d_n/R)] \tag{6a}$$

with

$$U_\infty = R(\partial U_\parallel/\partial n)_{d_n=0}. \tag{6b}$$

The relationship for the wave speed of the disturbance [Eq. (4.12) in the FW model], that in our notations corresponds to the additional tangential velocity of the cell tips due to convection V_{tC}, reads as

$$V_{tC}/V_n = \mathrm{Re}_n\, H^*(k, \hat{\gamma}), \tag{7}$$

where $\mathrm{Re}_n=U_\infty/V_n$ is the Reynolds number (V_n is the local normal velocity of the interface) and $H^*(k,\hat{\gamma})$ is a function that depends on the partition coefficient k and on the nondimensional wave number of the perturbation $\hat{\gamma}=\sqrt{2}\frac{2\pi}{\lambda}l_s(r)$ with $l_s(r)=D/V_n(r)$ the local solutal length. The detailed expression for $H^*(k,\hat{\gamma})$ is given in Ref. [14] by Eq. (4.13), together with Eqs. (4.8), (4.10), and (4.11). As dilute succinonitrile-water alloys are in the limit of a partition coefficient k approaching zero [20], Eq. (7) can be reduced to

$$V_{tC} = U_\infty\{2 - [\sqrt{(\hat{\gamma}^2 + 1/4)} - 1/2](2\hat{\gamma} + 1)/\hat{\gamma}^2\}. \tag{8}$$

The values of all the numerical parameters used in the calculations are summarized in Table I. Finally, we find from Eq. (8) that the traveling wave associated to convection is moving forward inducing an additional tangential contribution to the cell velocity, V_{tC} of 0.43 μm/s for $V_P=10$ μm/s and 5.5 μm/s for $V_P=20$ μm/s, which due to projection in view from the top [Eq. (3)] results in a slightly lower additional tip gliding velocity, $V_{rA,C}$ equal to 0.42 μm/s and 4.8 μm/s, respectively. It is worth noting that, in the region of the interface around the inception of cells from morphological instability, these values are of the same order as the discrepancy in Fig. 3 between the experimental tip velocity and the theoretical one resulting from advection by the slope only ($\sim$1 μm/s for $V_P=10$ μm/s and $\sim$10 μm/s for $V_P=20$ μm/s). The hypothesis of convection-driven cell advection is receiving theoretical support for both its direction and order of magnitude.

IV. CELLULAR PATTERN CHARACTERIZATION

As already mentioned, curvature is associated to a microstructure gradient from smooth interface at the crucible boundary to large cells in the center. It is therefore of value to determine the variation of the average cell surface with radial position. For this, the cellular array is divided into concentric rings that are characterized individually in terms of average cell size, number of cells, neighboring of cells, and so on (Fig. 6). The cell surface directly measured on

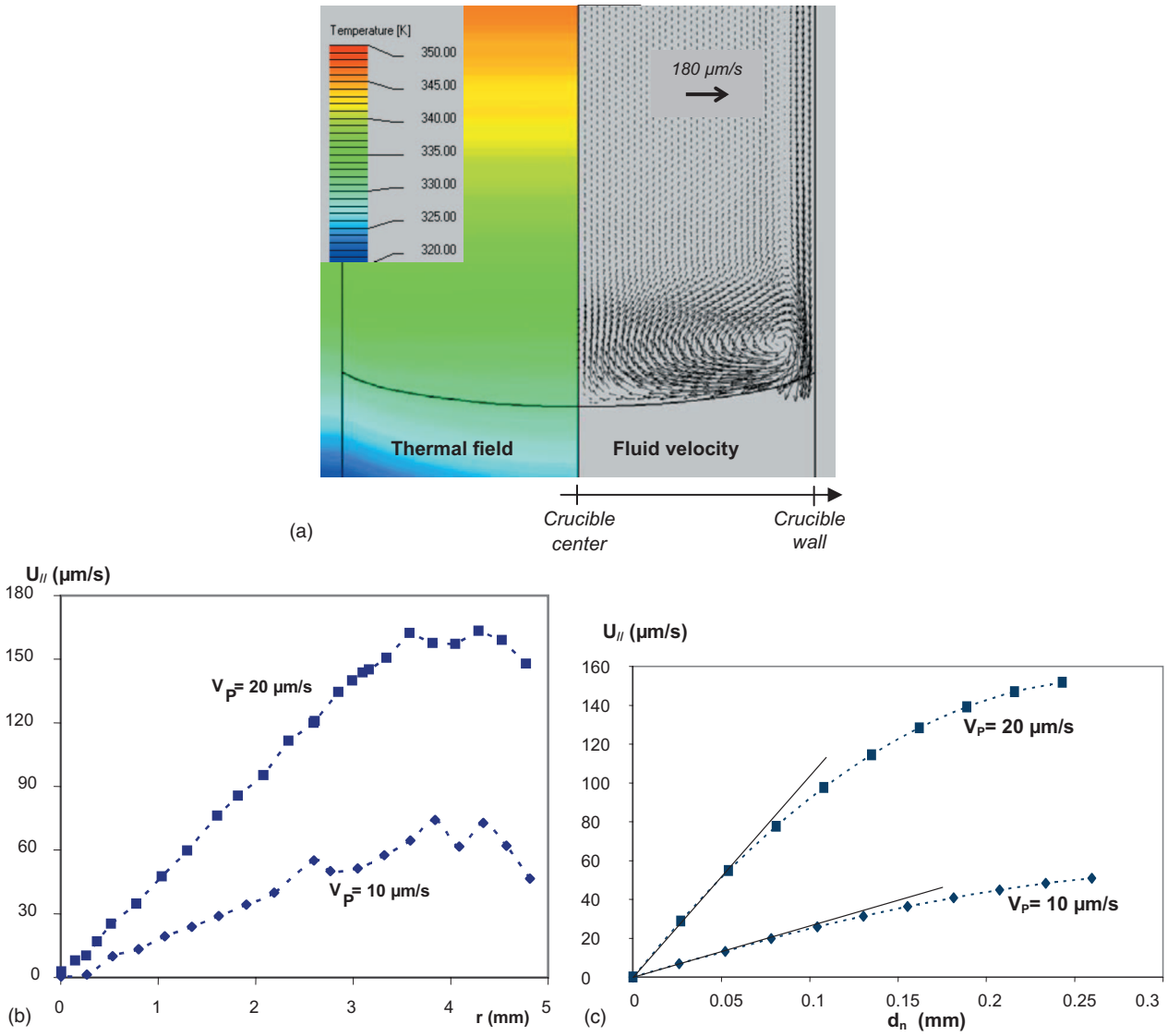

FIG. 5. (Color) Analysis of CrysVUn® simulations of the fluid velocity fields for $V_P=10$ μm/s and $V_P=20$ μm/s. (The temperatures of the furnace areas are the same for all simulations but the measured resulting gradient in the liquid at the center of the interface slightly differs: $G=25$ K/cm at $V_P=10$ μm/s, $G=21$ K/cm at $V_P=20$ μm/s.) (a) Example of the temperature and fluid velocity fields ($V_P=20$ μm/s). (b) Variation of the tangential component of fluid velocity along the interface, taken at a normal distance of 250 μm from the interface. (c) Variation of the tangential component of fluid velocity along the direction normal to the interface, taken roughly at the birthplaces of cells ($r=2.5$ mm for $V_P=10$ μm/s, $r=3.5$ mm for $V_P=20$ μm/s). The slope at the origin, used to determine U_∞, is also shown.

top-view images is corrected to take into account the interface slope that tends to reduce the apparent surface size compared to the real one. It is clear that the inner the ring the lower the number of cells and the larger the standard deviation (Fig. 7).

If we consider only the effect of lateral drift by the slope applied to the ring of cells that appear at one time t on the periphery of the unstable area, on a concave interface, cells are expected to shrink during their motion towards the central sink in both radial and azimuthal directions. Indeed, if array dynamics is neglected:

(i) The number of cells on a circle of radius r remains constant while its perimeter $2\pi r$ is continuously reducing during the advection towards the center.

(ii) It follows from the decrease of the gliding rate towards the center of the interface pointed out in Fig. 3 that the highest groove of a cell has a higher velocity than the lowest groove, which leads to the following relationship for the variation of the cell area $A(r)$ in gliding over a parabolic interface:

$$A(r) = A_0 \frac{r^2}{r_0^2} \tag{9}$$

with A_0 as the cell area at the cell inception at r_0.

This situation is opposite to what is observed on a convex interface where the slightly smaller advection velocity of the upper cell groove makes it lagging behind the lower one,

TABLE I. Numerical parameters used for the calculations.

Experimental data	For $V_P=10$ μm/s ($r=2.5$ mm)	For $V_P=20$ μm/s ($r=3.5$ mm)
Average cell area S	5300 μm^2	5100 μm^2
Characteristic cell dimension $\lambda=\sqrt{S}$	73 μm	71 μm
Local normal velocity of the interface V_n	9.82 μm/s	17.5 μm/s
Estimated fluid velocity U_∞ [from Eq. (6b)]	1200 μm/s	5100 μm/s
Reynolds number Re_n	127	292
Gliding velocity due to convection $V_{rA,C}$	0.42 μm/s	4.8 μm/s
Physical parameters		
Diffusion coefficient in liquid D	2.22×10^{-9} m^2/s [21]	
Partition coefficient k	~0	
Viscosity	2.6×10^{-6} m^2/s (SCN data: [22])	
Schmidt number	1170	

which with time results in cyclic cell stretching and division [3]. However, this analysis is clearly not correct as pattern dynamics leading to coarsening and elimination must be taken into account. To analyze the relative importance of those two phenomena (advection and pattern dynamics), we use the simple relationship, Eq. (9), elaborated above, of cell size evolution along the interface that only include slope advection. This calculation makes use of the expression of the theoretical gliding velocity due to the interface curvature, Eq. (2). The comparison with real cell size evolution will help us to understand the contribution of pattern dynamics. Results of this model for $V_P=20$ μm/s are superposed to experimental results in Fig. 7 and it appears that the expected decrease of cell surface is observed for the border rings only. Then, the cell surface first stabilizes before largely increasing again as the center is approached.

Actually, two effects are competing: Global array advection down the interface, which tends to decrease the cell size, while cell elimination during array ripening [23,24] is favoring coarsening of the average cell surface as on a usual flat interface. Towards the periphery, the cell array has just formed and the interface slope is large so that array ripening is comparatively negligible and cell advection dominant. Conversely, in the central rings, where the interface slope

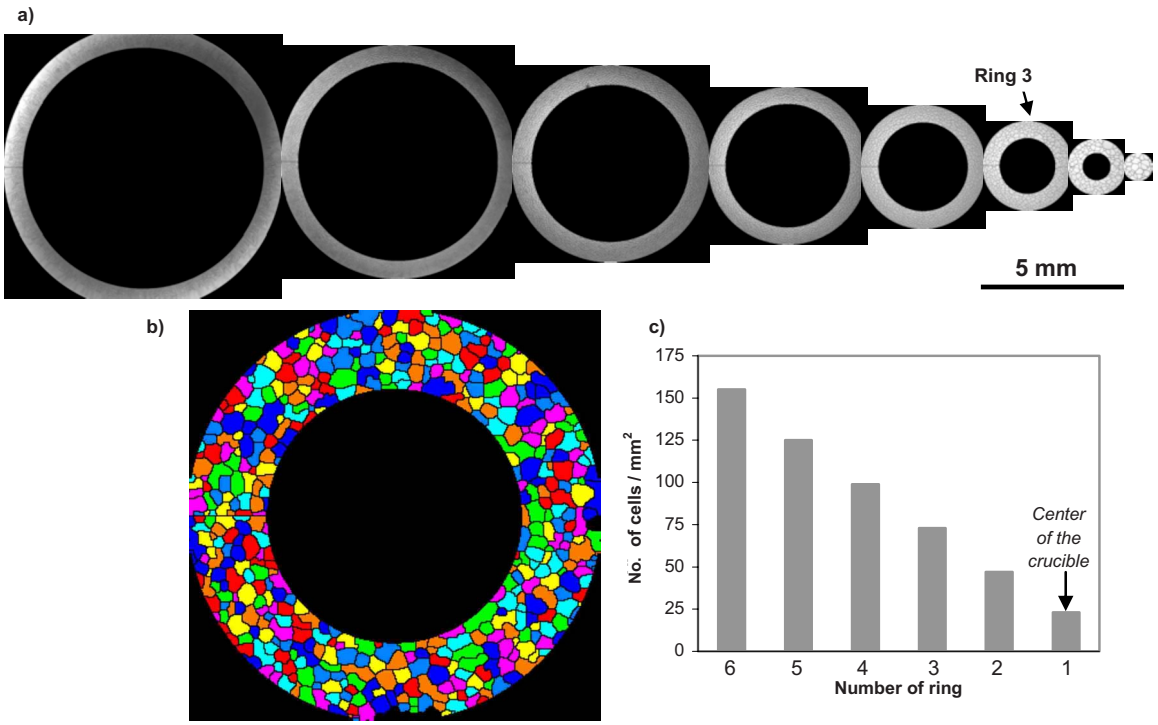

FIG. 6. (Color online) Cell surface analysis. (a) Rings used for measuring the cell area at $V_P=20$ μm/s. (b) Analysis of cells for ring 3. (c) Variation of the number of cells per unit area along the interface.

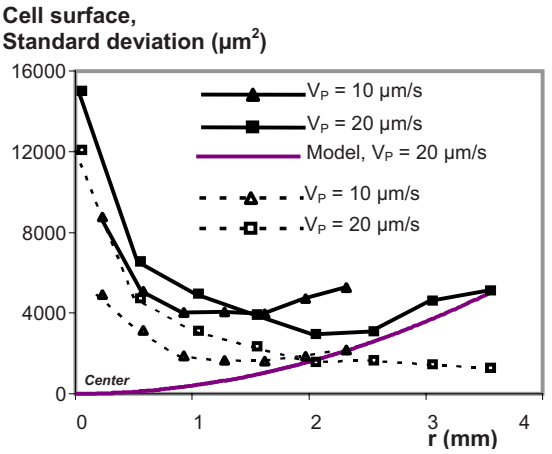

FIG. 7. (Color online) Variation of the average cell surface $A(r)$ (▲, ■) and standard deviation (△, □) with the distance from the center, extracted from the cell surface histograms. The theoretical evolution of the cell surface calculated using Eq. (9) is also drawn for V_P=20 μm/s.

and gliding velocities are the weakest (V_{rA} is decreasing to zero), regular array ripening becomes dominant, and massive cell elimination is visible by comparing, for example, the numbers of cells per unit area on each ring [Fig. 6(c)]. The intermediate region where the cell surface is about constant merely corresponds to the crossover between the two limit regimes.

V. CONCLUSION

The complex dynamics of a cellular pattern on a naturally concave solid-liquid interface is observed *in situ* during the 3D-directional solidification of a succinonitrile-water alloy in a cylinder, and analyzed in details. A spectacular phenomenon of global pattern advection is brought out which results from the collective gliding of the cells down the interface slope. This cell advection is generating a source-sink process as the cells are gliding from the circular border region of the interface, where they were born from morphological instability, towards the center, where they get buried. The comparison of the experimental gliding rate of the cells, which varies over the interface, with the theoretical one imposed directly by the local interface slope reveals a misfit. As fluid flow driven by heat losses into the glass crucible wall is significant for transparent organic alloys, this misfit is attributed to an additional contribution to cell gliding, driven by convection. A rough estimation of this effect, based on an adaptation of a model developed by Forth and Wheeler [14] to analyze the effect of fluid flow on the characteristics of morphological instability at the onset, supports this hypothesis.

The present observations of cell array dynamics on a concave interface are essentially different from and thus complementary to those of previous studies on 2D systems presenting a convex curvature [3,4]. Apart from the influence of convection, pattern dynamics is drastically modified in our 3D configuration with a concave interface. On the one hand, the continuous drift of the cells from the source to the sink, which in combination with cell coarsening produces irregular arrays, is replacing the regular organization of the interface pattern that form on convex 2D interfaces due to the periodic attractor associated to repetitive cell stretching and splitting. On the other hand, on a concave interface, the decrease of the cell size due to cell contraction, caused by both slope advection and reduction in 3D samples of the space available per cell linked to the cell-ring perimeter decrease when gliding towards the center, is competing with usual cell coarsening. It is shown that in the cell-size evolution with time there is a crossover from a regime dominated by advection to a regime dominated by coarsening. Finally, only a few large cells survive coarsening and reach the central area. This very complex source-sink dynamics, ending with coarsening and large standard deviation of cell size, seems incompatible with the formation of regularly organized patterns.

To get further insight in the phenomena, it would be worth to analyze the dynamical effects induced by a macroscopically concave interface on cellular arrays without bias from fluid flow driven by gravity in the melt. Therefore, a comparative study in the reduced-gravity environment of space, whose objective is to characterize the solid-liquid interface microstructure while directional solidification experiments are performed, is planned over the forthcoming years in the DECLIC DSI onboard the International Space Station.

Furthermore, this *in situ* study on 3D samples of cellular pattern dynamics on a concave solidification interface, and in particular the changes noticed with the convex-interface case, strongly support the interest of monitoring the macroscopic interface curvature in 3D so as to control its sign and amplitude, and then follow the changes in the dynamics of cellular pattern advection and in array organization. To complement the present results, two cases would be most interesting: A macroscopically planar interface to get a reference cellular pattern (no slope advection) and a convex macroscopic interface. Therefore, a small device designed to flatten the interface by local heat injection close to the solid-liquid interface has been recently installed on our laboratory furnace [25], and work is currently in progress. Another critical point would be to analyze the influence of the type of interface microstructure, and more especially of its depth, on pattern advection dynamics. Indeed, the cells are rather shallow in the present study [see Figs. 1(a) and 1(c)] that is likely to favor high lateral mobility, whereas some anchoring of the cell walls is expected to manifest itself for deeper cells, with unknown consequences on cell gliding.

ACKNOWLEDGMENTS

The authors express their gratitude to the French Space Agency (CNES) and the European Space Agency (ESA) for the support received in the MISOL3D (Microstructure de Solidification 3D) project of CNES and the CETSOL (Columnar-Equiaxed Transition in Solidification processing) project of ESA.

[1] M. C. Cross and P. C. Hohenberg, Rev. Mod. Phys. **65**, 851 (1993).
[2] S. R. Coriell, R. F. Boisvert, G. B. McFadden, L. N. Brush, and J. J. Favier, J. Cryst. Growth **140**, 139 (1994).
[3] S. Bottin-Rousseau and A. Pocheau, Phys. Rev. Lett. **87**, 076101 (2001).
[4] A. Pocheau and S. Bottin-Rousseau, Chaos **14**, 882 (2004).
[5] H. Jamgotchian, N. Bergeon, D. Benielli, P. Voge, and B. Billia, J. Microsc. **203**, 119 (2001).
[6] N. Noël, F. Zamkotsian, H. Jamgotchian, and B. Billia, Meas. Sci. Technol. **11**, 66 (2000).
[7] H. Jamgotchian, N. Bergeon, D. Benielli, P. Voge, B. Billia, and R. Guérin, Phys. Rev. Lett. **87**, 166105 (2001).
[8] Y. J. Chen and S. H. Davis, J. Fluid Mech. **421**, 369 (2000).
[9] C. W. Lan, Y. W. Yang, H. Z. Chen, and I. F. Lee, Metall. Mater. Trans. A **33**, 3011 (2002).
[10] M. Kurz, Ph.D. thesis, Technical University Erlangen-Nürnberg, 1998.
[11] M. Kurz, A. Pusztai, and G. Müller, J. Cryst. Growth **198-199**, 101 (1999).
[12] See EPAPS Document No. E-PLEEE8-79-041901 for a video showing cellular-pattern advection at a concave solid-liquid interface during directional solidification of a succinonitrile −0.3 wt % water alloy in a cylindrical glass tube of 10 mm inner diameter (V_P=20 μm/s, G=30 K/cm, *in situ* bright-field observation from the top). For more information on EPAPS, see http://www.aip.org/pubservs/epaps.html.
[13] T. Huang, S. Liu, Y. Yang, and Y. Zhou, J. Cryst. Growth **128**, 167 (1993).
[14] S. A. Forth and A. A. Wheeler, J. Fluid Mech. **202**, 339 (1989).
[15] S. A. Forth and A. A. Wheeler, J. Fluid Mech. **236**, 61 (1992).
[16] S. R. Coriell, G. B. Mc Fadden, and R. F. Boisvert, J. Cryst. Growth **69**, 15 (1984).
[17] R. T. Delves, J. Cryst. Growth **3-4**, 562 (1968); **8**, 13 (1971).
[18] K. Murakami, T. Fujiyama, A. Koike, and T. Okamoto, Acta Metall. **31**, 1425 (1983).
[19] R. Tönhardt and G. Amberg, J. Cryst. Growth **194**, 406 (1998).
[20] J. E. Smith, Z. O. Frazier, and W. F. Kaukler, Scr. Metall. **18**, 677 (1984).
[21] X. Wan, Q. Han, and J. D. Hunt, Metall. Mater. Trans. A **29**, 751 (1998).
[22] P. Tin and H. C. de Groh, Int. J. Thermophys. **25**, 1143 (2004).
[23] J. A. Warren and J. S. Langer, Phys. Rev. E **47**, 2702 (1993).
[24] W. Losert, B. Q. Shi, and H. Z. Cummins, Proc. Natl. Acad. Sci. U.S.A. **95**, 439 (1998).
[25] N. Bergeon, R. Trivedi, B. Billia, B. Echebarria, A. Karma, S. Liu, C. Weiss, and N. Mangelinck, Adv. Space Res. **36**, 80 (2005).